SAND2011-9367 C

SAND2011-9367C

Characterization of Controlled Perturbations in a Hypersonic Boundary Layer

Katya M. Casper*

School of Aeronautics and Astronautics, Purdue University, West Lafayette, IN 47907-1282

Sandia National Laboratories, Albuquerque, NM 87185

Steven J. Beresh†

Sandia National Laboratories, Albuquerque, NM 87185

Steven P. Schneider‡

School of Aeronautics and Astronautics, Purdue University, West Lafayette, IN 47907-1282

A study was conducted to better characterize the flow perturbations used to generate instability waves and turbulent spots on the nozzle wall of the Boeing/AFOSR Mach-6 Quiet Tunnel. A high-voltage probe and current transformer were used to measure the flow perturbations. Instead of creating an arc discharge as expected, the perturber was found to generate a pulsed glow. In order to characterize the initial formation of disturbances generated by the glow discharge, spanwise measurements were made near the perturber location. A low-frequency pressure disturbance was measured. However, higher frequency second-mode waves at that location were too small to be resolved above the background electronic noise levels.

Also, the repeatability of the instability wave packets and turbulent spots generated by the glow was measured. Similar results were obtained when a duplicate electrode was used, the perturber polarity was flipped, or the electrode was rotated by ninety degrees. Repeatability was also shown when upstream sensor inserts were removed and replaced by contoured blanks. Finally, the axisymmetry of the nozzle-wall flow was studied by moving the setup to the bottom wall of the tunnel. Instability waves had 15–20% higher frequencies and grew more quickly on the bottom wall. These trends were consistent with temperature stratification in the tunnel.

Nomenclature

Φ	power-spectral density ($(p'/p_\infty)^2/Hz$)	T_0	tunnel stagnation temperature (K)
θ	tunnel azimuthal angle, looking upstream	U_∞	freestream velocity (m/s)
θ_e	rotation angle of perturber electrodes	x	axial coordinate (m)
f	frequency (kHz)	y	tunnel spanwise coordinate measured from top wall of the tunnel along the circumference of the wall, looking upstream (mm)
M	freestream Mach number		
p'	pressure fluctuation, $p - p_\infty$ (Pa)		
p_∞	freestream static pressure (Pa)	z	tunnel axial coordinate measured from throat (m)
P_0	tunnel stagnation pressure (kPa)		
Re	freestream unit Reynolds number (1/m)		

*Research Assistant and Sandia Graduate Intern, Student Member AIAA, kcasper@purdue.edu, (765) 494-3348

†Principal Member of the Technical Staff, Engineering Sciences Center, Associate Fellow AIAA

‡Professor, Associate Fellow AIAA

Sandia National Laboratories is a multi-program laboratory managed and operated by Sandia Corporation, a wholly owned subsidiary of Lockheed Martin Corporation, for the U.S. Department of Energy's National Nuclear Security Administration under contract DE-AC04-94AL85000.

I. Introduction

Hypersonic reentry vehicles are subjected to high fluctuating pressures. These intense fluctuations can cause vibration of internal components and lead to structural problems. There is a need to predict the magnitude, location, and spatial extent of the pressure fluctuations to better design hypersonic flight vehicles. Current designs often use overly conservative estimates of the fluctuations that can lead to heavier vehicles and degraded flight performance. Some correlations exist for the magnitude of transitional and turbulent pressure fluctuations, but these were derived primarily using either incompressible data or conventional (noisy flow) hypersonic wind-tunnel tests.[1] Too little physical understanding of the generation of transitional pressure fluctuations has resulted from such modeling efforts.

Wind-tunnel tests at fixed freestream conditions have shown that transitional pressure fluctuations can be more severe than turbulent pressure fluctuations,[2–6] making transitional fluctuations of primary interest for this work. The transition process can be described through intermittency and the growth and propagation of turbulent spots in the transitional boundary layer.[7] These turbulent spots create wall pressure fluctuations. By combining the pressure fluctuations associated with wave packets and turbulent spots into a model of transition, transitional pressure fluctuations can be calculated from fundamental physics. This type of model has already been developed for incompressible flow on a flat plate.[8] Recent direct numerical simulation (DNS) efforts have computed the pressure field for wave packets and developing turbulent spots in hypersonic boundary layers.[9–12] Recent experimental measurements have also measured the internal structure of spots in pressure data under a hypersonic boundary layer.[13,14] These measurements were made on the nozzle wall of the Boeing/AFOSR Mach-6 Quiet Tunnel (BAM6QT). Under quiet-flow conditions, laminar boundary layers are maintained on the wall of the wind tunnel. A perturber was used to create controlled perturbations on the nozzle wall. The resulting instability wave packets were measured along with their development into turbulent spots, including centerline and spanwise measurements.

The current work focuses on better characterizing these experiments. Current and voltage measurements were made of the input perturbation to the flow. These show the frequency content of the perturbations. Also, pressure measurements were made further upstream to characterize the disturbances in the near-field of the perturber. Both efforts are to be used to improve DNS computations by supplying more information about the input perturbation. Finally, repeat experiments were conducted to define the sensitivity of experiments to changes in the electrodes and the nozzle-wall inserts. The axisymmetry of the nozzle-wall boundary layer was also studied.

II. Experimental Setup

A. Boeing/AFOSR Mach-6 Quiet Tunnel

Measurements were made on the nozzle wall of the Boeing/AFOSR Mach-6 Quiet Tunnel (Fig. 1). This tunnel is one of two hypersonic quiet tunnels in the world. Because it can be operated as a conventional noisy tunnel or as a quiet tunnel, freestream noise effects can be studied. The tunnel is a Ludwieg tube – a long pressurized tube with a converging-diverging nozzle on the end. The flow passes from the driver tube, through the test section, diffuser, and finally to the vacuum tank. Flow is initiated by bursting a double diaphragm that is located downstream of the diffuser. When the flow begins, an expansion wave travels upstream and then reflects between the upstream end of the driver tube and the contraction. The total pressure and temperature drop with each reflection cycle (every 200 ms) until the tunnel unstarts. Run times of 3–5 s under quiet-flow conditions are typical at present. The tunnel uses air as the test gas and operates with an initial total pressure P_0 of 34–2070 kPa and an initial total temperature T_0 of 430 K. These conditions give a freestream unit Reynolds number range of $0.4–18.3 \times 10^6$/m, calculated using Keyes's law for viscosity.[15] The current maximum quiet stagnation pressure is 1170 kPa. The test-section diameter is 0.242 m at the nozzle exit, and the nozzle is 2.590 m long. Noise levels vary from 2–4.5% under noisy-flow conditions. Under quiet-flow conditions, noise levels are 0.05% or less.[16]

Obtaining quiet flow in a hypersonic tunnel is not a trivial task. The nozzle is polished to a mirror finish to avoid roughness-induced transition, and the contraction boundary layer is also removed by bleed slots at the throat. A new laminar boundary layer then begins just upstream of the nozzle throat and is maintained through the test section. In addition, the air is filtered to remove dust or other particles above 0.01 microns that may damage the nozzle or trip the boundary layer. More details about the development of the BAM6QT can be found in Schneider.[17]

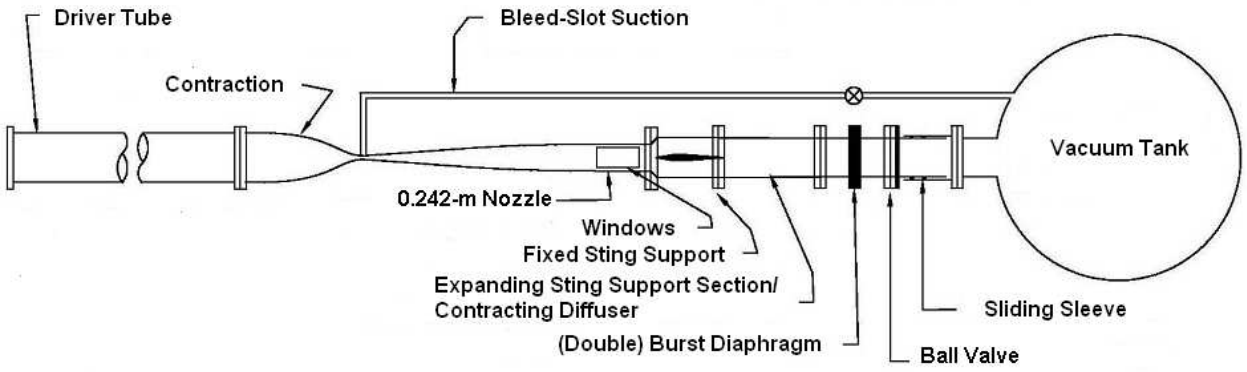

Figure 1. Boeing/AFOSR Mach-6 Quiet Tunnel

B. Controlled Generation of Wave Packets and Turbulent Spots using a Flow Perturber

A flow perturber is used to generate instability wave packets and turbulent spots within the length of the test section. The perturber uses an electrode design that isolates the ground from the tunnel, reducing the generation of electrical noise. This design has two 1.1-mm diameter stainless steel electrodes in a Macor mount. The gap between electrodes is 1.3 mm and is typically oriented perpendicular to the flow. An ignition coil and timing circuit is used to create perturbations. The ignition coil always remains charged. When the coil is suddenly shut off, a perturbation is created. This is typically repeated at 200 Hz to allow measurements of the resulting disturbances in the intervals between the electro-magnetic interference generated by the perturbation.

C. Instrumentation and Data Acquisition

Kulite XCQ-062-15A pressure transducers are used to measure surface pressure fluctuations. These transducers use silicon diaphragms as the basic sensing mechanisms. Each diaphragm contains a fully active four-arm Wheatstone bridge. The sensors are mechanically stopped above 103 kPa to prevent damage to the diaphragms at the high BAM6QT pre-run pressures. They have a resonant frequency of 250–300 kHz. The repeatability of the sensors is approximately 0.1% of the full scale, or 0.1 kPa. The Kulites have screens to protect the diaphragms from damage. For these tests, only A-screen sensors were used. The A-screen has a large central hole. This screen offers only a small amount of diaphragm protection, but the sensor has a flatter frequency response up to 30–40% of the resonant frequency.[18] The sensitive area of the A-screen sensor is the hole size (0.81 mm^2). The Kulites are only used to obtain the AC signal. The sensors have a repeatable, linear calibration slope which can be used to determine the fluctuating component of the signal (within the flat dynamic range of the sensor).[19] The fluctuations were normalized by the freestream pressure, computed using the total pressure and freestream Mach number in the tunnel.

The signal from the Kulite pressure transducers was processed by custom-built electronics, which also supply a 10 V excitation. The output signal was amplified by a gain of 100 with an INA103 instrumentation amplifier chip to give the DC signal. Tektronix TDS7104, DPO7104, two TDS5034B, and two DPO7054 Digital Phosphor Oscilloscopes were used for data acquisition. The scopes have an 8-bit vertical resolution, but the resolution can be increased to over 11 bits in Hi-Res mode. Hi-Res mode is also used to provide digital filtering. The oscilloscopes average in real time at the maximum sampling rate of 1.25–5 GS/s (depending on the model) for 4 input channels and then save data at the specified sampling rate. The data sampling rate for these measurements was 500 kHz. Pressure traces were post-processed by low-pass filtering the data at 175 kHz using an 8-pole digital Butterworth filter (48 dB of attenuation per octave). This filtering removes sensor diaphragm resonance from the pressure traces to show the underlying data more clearly.

D. Apparatus

A schematic of the experimental setup is shown in Fig. 2. The perturber is placed on the top wall of the tunnel at z = 1.924 m, where z is the axial tunnel coordinate measured from the throat. There is a small spanwise insert at z = 2.055 m, downstream of the perturber electrodes (Fig. 3(a)). This spanwise insert has locations for sensors at y = ± 2.5, 5.1, 7.6, 10.1, 15.2, and 20.2 mm, where y is measured from the centerline of the perturber position along the circumference of the wall. Downstream, there are various sensor locations along the tunnel centerline in a slender traverse plug insert. There is also a cylindrical pipe insert that was designed to fit between the nozzle exit and the diffuser sting support as shown in Figs. 2 and 3(b). This insert has the same diameter of 0.242 m as the nozzle exit. When the tunnel is closed, the pipe insert fits flush with the nozzle exit and extends 0.254 m downstream. This pipe insert is actually made of five rings. One of the downstream rings has azimuthal sensor locations at y = ± 11, 21, 32, 42, and 63 mm. The four downstream rings are interchangeable to allow azimuthal measurements at any of the four downstream locations. For these measurements, the spanwise array of sensors was located at z = 2.781 m.

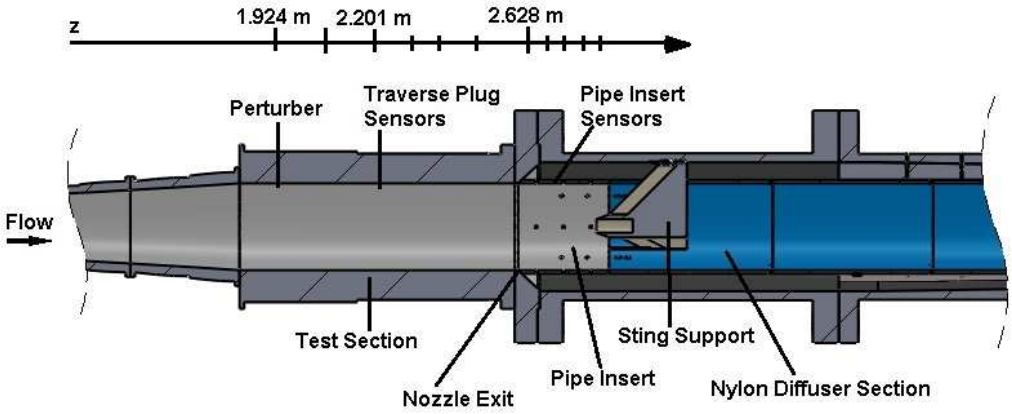

Figure 2. Schematic of experimental setup in the BAM6QT for nozzle-wall measurements. Perturber and sensor locations are marked on the z axis.

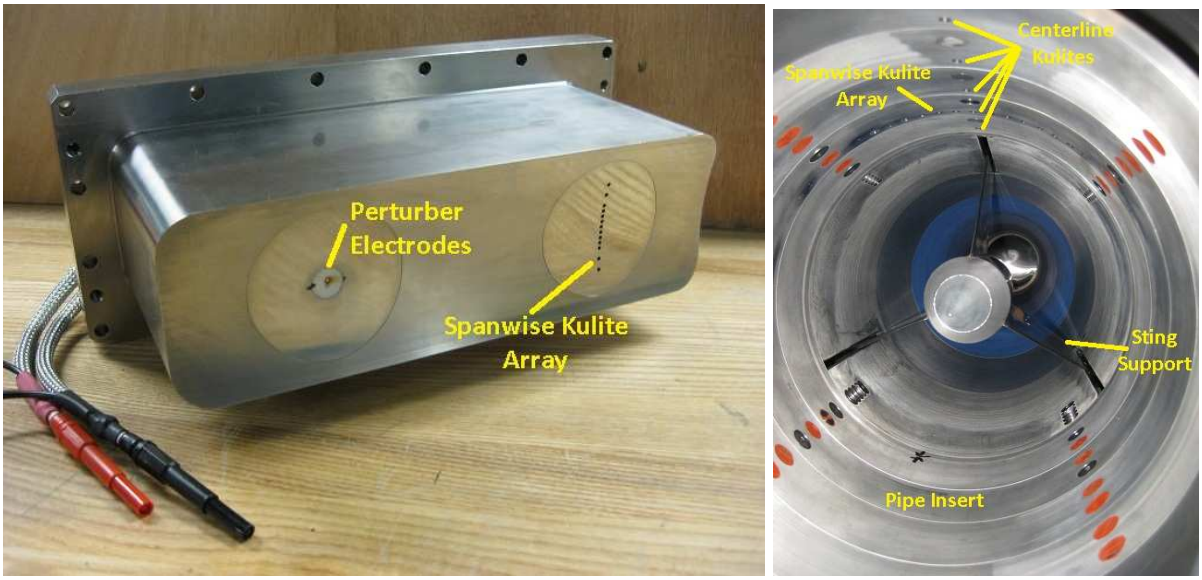

(a) (b)

Figure 3. Pressure instrumentation inserts; (a) Upstream insert; (b) Downstream pipe insert.

III. Experimental Results

A. Measurements of Perturbation

During initial experiments, it was assumed that the flow perturber was consistently creating spark perturbations.[13,14] Repeatable instability wave packets were created and studied as they broke down into turbulent spots. However, during a typical run (consisting of 600 perturbations) several abnormally large perturbations would occur. These large perturbations were accompanied by significant electrical noise that created a residual low-frequency decay in the Kulite pressure data. At low Re, only a few of these large perturbations tended to occur. As the Re was increased, more and more would occur, especially during the first 0.25 s of perturber operation. It was unclear if the electronic noise accompanying these perturbations would couple with the pressure signal and affect the data. To avoid this possibility, the large perturbations were identified using a threshold criteria, and pressure data following them were not used for data analysis. The remaining smaller perturbations and resulting boundary-layer disturbances were retained.

In order to better characterize the perturbation being applied to the flow, voltage and current measurements were made. The current across the electrodes was measured using a Bergoz CT-D1.0 current transformer. This current transformer has a sensitivity of 1V/A and can resolve frequencies between 200 Hz and 500 MHz. It can measure a maximum current of 1000 A and a maximum root-mean-square (RMS) fluctuating current of 11 A. The voltage across the electrodes was measured using a Tektronix P6015 High-Voltage Probe. This is a 1000× attenuator probe that can resolve frequencies between 0 and 75 MHz. Voltages up to 20 kV DC or 40 kV RMS can be measured. The voltage was measured between the electrode wires running from the perturber. The sampling rate was typically 5 MHz. Together, these measurements give the current and voltage of the perturbation as a function of time, allowing computation of the perturbation power and energy. However, possible electro-magnetic interference adds some uncertainty to these measurements.

Fig. 4 shows the voltage, current, and power measurements at a low, intermediate, and high Re. The freestream conditions are similar to previous experiments.[13,14] These results show the typical small perturbations that were used for all data analysis; large perturbations that intermittently occurred were removed using a threshold criteria on the data. These results are an ensemble average of 50 samples. A surprising result is seen in these measurements. A low frequency pulse in voltage and current is observed instead of a rapid spark. Also, the voltage is too high and the current is too low for an arc discharge. The measured voltage and current actually lie within the expected range for a glow discharge. Therefore, it seems that the boundary-layer disturbances measured further downstream by Kulite pressure transducers are created by a pulsed glow discharge, not the expected spark perturbation. As Re increases, the current amplitude associated with the perturbation increases as shown in Fig. 4(a). However, the voltage amplitude decreases (Fig. 4(b)). Overall, these opposite trends result in a smaller power and energy of the perturbation (Fig. 4(c)). Table 1 shows the energy for the various freestream conditions in these experiments. As the Re is increased, the energy decreases to 86% of its value at Re = 5.70 $\times 10^6$/m.

Table 1. Ensemble-averaged perturbation energy for varying Re.

Re $\times 10^6$/m	Energy (mJ)	% of Maximum Energy
5.70	12.33	100
6.41	11.79	96
7.09	11.67	95
7.70	11.61	94
8.43	11.20	91
9.01	11.11	90
9.62	10.94	89
10.3	10.81	88
10.9	10.66	86

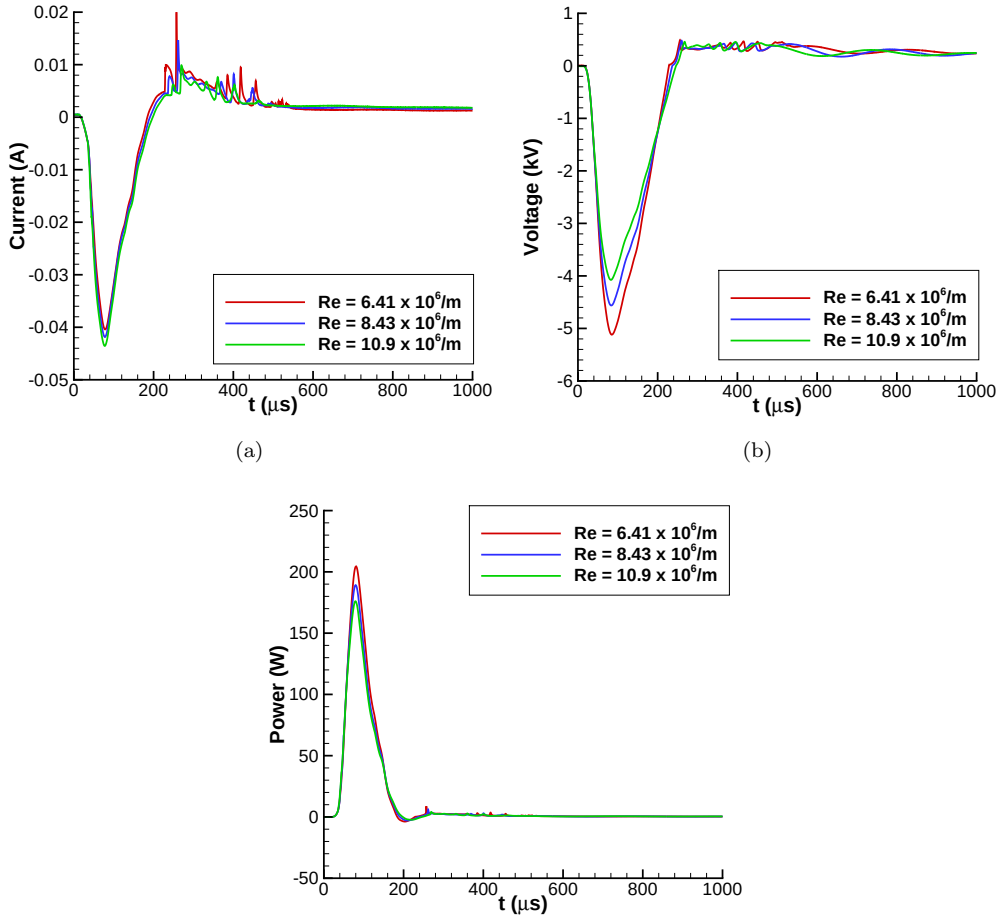

Figure 4. Ensemble-averaged perturbation measurements at varying Re (a) Current; (b) Voltage; (c) Power.

This pulsed glow is not a rapid impulse. Instead, it is a lower frequency, high energy perturbation. A power-spectral density (PSD) of the electrical perturbation was computed to show its dominant frequency content (Fig. 5). FFT's of 50 perturbations were computed, and these were averaged and normalized to compute the PSD. The dominant frequencies in the spectra are below 30 kHz; however, there is frequency content that extends well above 150 kHz. These higher frequencies are several orders of magnitude smaller than the low-frequency peak, but still much larger than than the electronic noise in the system.

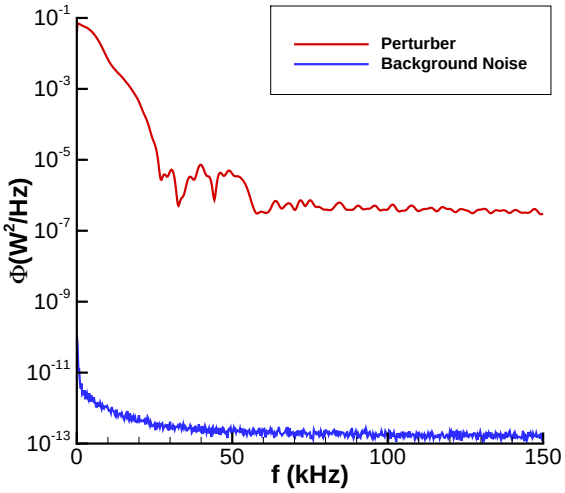

Figure 5. PSD of power measurements at $Re = 6.40 \times 10^6/m$**.**

These high frequencies come from rapid spikes in the perturbation. These high frequencies are most apparent when looking at individual samples as opposed to an ensemble average. Fig. 6(a) shows the glow pulse for Re of 6.40×10^6/m. 50 individual samples are shown along with the ensemble average. Deviation from the average appear during the initial rise in the power near t = 50 μs and also after the power peak near 500 μs. Boundary-layer disturbances are first measured downstream of the perturber at z = 2.055 m near t = 200 μs, so the source of the flow disturbances should originate before that time. A close-up view of the power near 50 μs is shown in Fig. 6(b). There is a high-frequency spike in the individual samples at the beginning of the glow pulse. This spike occurs primarily in the current of the perturbation. This nearly instantaneous jump adds a high-frequency component to the pulse, which may be the source for the second-mode frequencies. However, there is uncertainty as to what causes this spike and how the electrical perturbation couples with the flow. More analysis of these high frequencies and attempts to correlate the jitter and amplitude of the high frequencies to the second-mode waves downstream will be conducted in future analyses.

These measurements contrast with those shown in Fig. 7. Fig. 7(a) shows voltage measurements of a single electrical perturbation, but with a shorter time scale. A decrease in voltage is again seen between 0 and 200 μs, corresponding to a pulsed glow perturbation. However, this voltage dip has two large superimposed spikes near t = 35 and 50 μs. These spikes correspond to the large perturbations that intermittently create large amounts of electrical noise in the pressure measurements. Fig. 7(b) show a close-up view of the second voltage spike. The spike is a low voltage, high-frequency oscillation, which seems to correspond to an arc discharge. Current measurements were also made of this electrical perturbation (Fig. 7(c)). The time scale is again shorter compared to Fig. 4. Also, the scale of the current measurement is over two orders of magnitude larger in order to resolve the large current spikes near t = 35 and 50 μs. The current measurements do not show the small current associated with the pulsed glow because of the resolution of the measurements; the vertical scale was much larger and the sampling rate for these measurements was an order of magnitude larger (2.5 GHz) in order to resolve the short spikes. Fig. 7(d) shows a close-up view of the second spike which again shows a high-amplitude oscillatory current. In this case, two sparks occur during the glow. However, the number of sparks is not repeatable; a single trigger might result in as many as ten sparks combined with a single glow discharge.

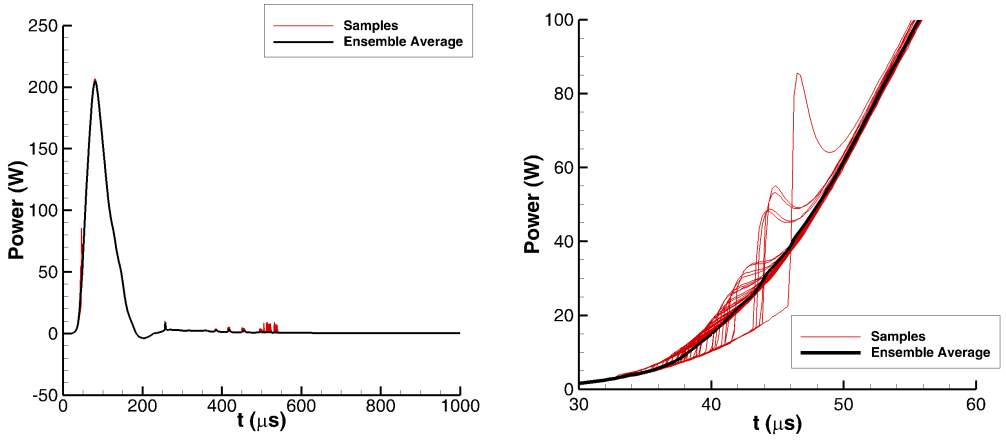

Figure 6. Power measurements showing high-frequency component of perturbation, $Re = 6.40 \times 10^6/m$ (a) Individual samples and ensemble averages; (b) Detail view a high-frequency spikes superimposed on the low-frequency glow pulse.

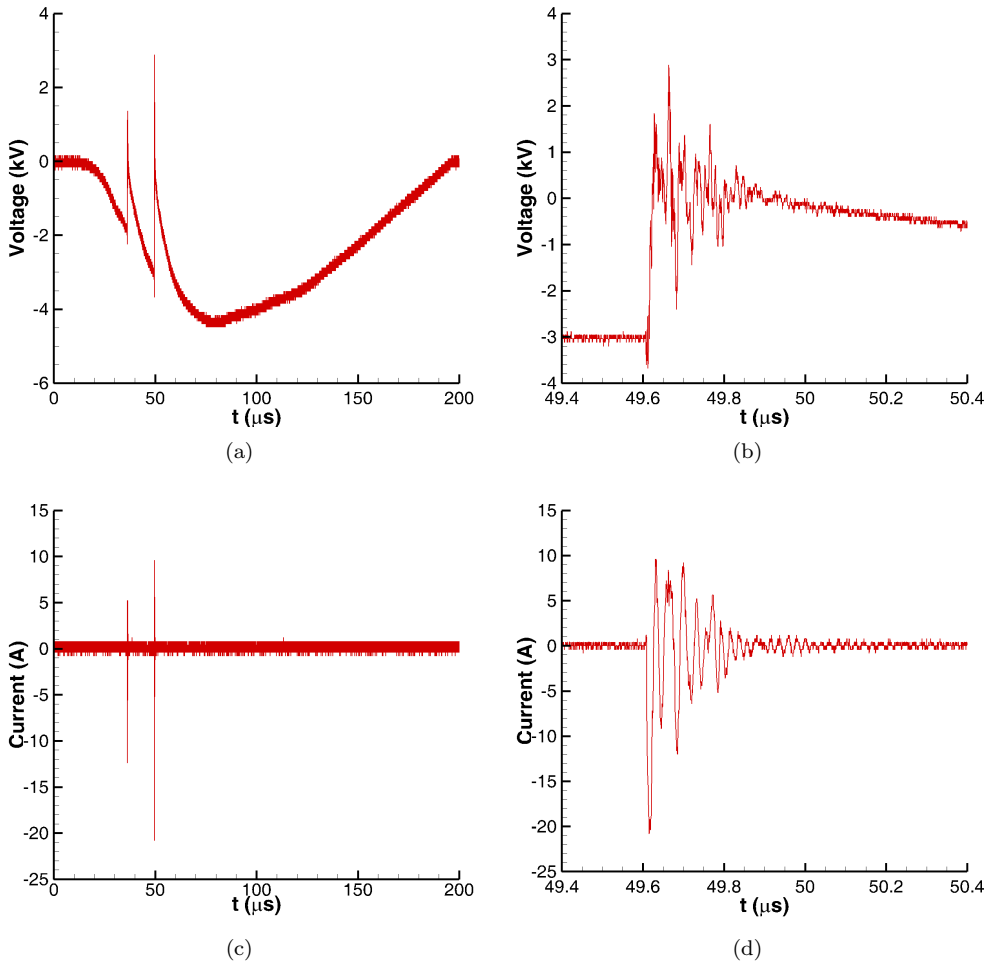

Figure 7. Flow perturbation measurements showing intermittent sparks superimposed on a glow perturbation, $Re = 5.60 \times 10^6/m$ (a) Voltage; (b) Voltage (detail of second spark); (c) Current; (d) Current (detail of second spark).

Visual confirmation of these results were obtained by imaging the perturbation on a cone model in the BAM6QT at Mach 6 (Fig. 8). A PCO.1600 camera with a 5 ms exposure was used to take black and white images of a single perturbation. Fig. 8(a) shows the two perturber electrodes in a Macor mount on the model. A glow region is seen above one of the electrodes (cathode) as a region of high intensity. The other electrode has no visible glow discharge around it and can only be seen because of a reflection of incoming light. Fig. 8(b) shows a glow discharge occurring simultaneously with a spark between the electrodes. When this spark occurs, large amount of electrical noise are created. A low-frequency component of the noise couples with the instrumentation and prevents useful data from being collected. These images confirm the current and voltage measurements discussed previously. Together, these measurements have shown that the flow perturber is actually used to create a pulsed glow, not an arc discharge. This glow creates controlled, repeatable perturbations without generating large amounts of electrical noise. The dominant frequency content of the pulse is below 30 kHz; however, there is also smaller broadband content at higher frequencies.

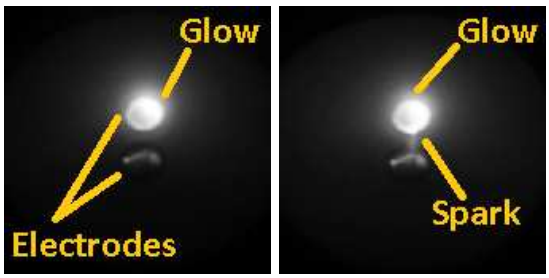

(a) (b)

Figure 8. Black and white pictures of flow perturbation on a cone model, $Re = 2.51 \times 10^6/m$**,** P_0 **= 255 kPa,** T_0 **= 427 K (a) Glow pulse; (b) Combined spark and glow pulse.**

B. Upstream Measurements

In order to better characterize the initial development of pressure disturbances created by the pulsed glow, spanwise measurements were obtained 0.131 m downstream of the perturber (z = 2.055 m) at varying Re. The pressure disturbances at this location are small; however, they show the initial growth of the disturbances before large second-mode instability wave packets and turbulent spots have developed. This measurement is also useful for DNS computations. Initially, the computations can compute the near-field of the perturber and adjust the input perturbation until it matches the experiments. Once a match is obtained, the full domain can be computed to compare to all the experimental results.

Because the perturbations were repeated at 200 Hz, multiple disturbances can be averaged to reduce electrical noise. The averaging trigger was the 200-Hz square-wave input signal to the perturber. Ensemble-averaged pressure traces of a 3-ms time period after the glow were computed for 50 disturbances. These traces were chosen from a 0.5-s interval of a run, after the perturber had been running for a few tenths of a second. More repeatable results were obtained after the perturber had warmed up. Also, even though Re drops within this 0.5-s interval, the change was smaller than 4% and no noticeable effects are seen in the results. Any disturbances that were contaminated by naturally-occurring turbulent spots or electrical noise from occasional spark discharges were not used in the averages. These cases occurred infrequently and were identified using an RMS threshold criteria on the laminar boundary-layer data measured by a single sensor between glow-induced disturbances. If a trace had a local RMS level greater than 10% of p_∞ (because of the presence of a naturally occurring turbulent spot), or if the mean level deviated more than 5% at the beginning or end of the trace (because of the low-frequency decay from electro-magnetic interference generated by a spark), then the disturbances were not used. An upstream nozzle-wall sensor was used for this check since glow-induced disturbances were still small and the majority of the measured pressure traces contained undisturbed laminar boundary layer data.

An ensemble-averaged power-spectral density (PSD) was also computed by averaging together the fast-Fourier transform (FFT) of each of the 3-ms pressure traces and normalizing to obtain the power-spectral density. This ensemble-averaged power-spectral density is not the same as taking a PSD of the ensemble-averaged pressure traces. This difference is most apparent when wave packets began to break down. Even though the packets show good repeatability while growing, their breakdown varies from packet to packet,

and the pressure fluctuations are no longer in phase. As a result, the ensemble-averaged pressure traces smooth out the turbulent fluctuations seen during breakdown. Since phase information is not contained in the FFT, ensemble averaging FFT's does not remove the large fluctuations during breakdown but instead creates an average representation of the frequency content of the individual samples.

Contour plots of the disturbances were also generated. An average convection velocity of $0.8U_\infty$ was used to convert the time traces to an approximate physical scale in order to generate a contour plot of the disturbances.[14] This result is an approximation since the leading and trailing edges of the spot convect at different velocities and the disturbance is changing as it convects downstream. However, it allows an approximate comparison of the spanwise and streamwise growth of the disturbances. When this conversion is used, earlier times will be further downstream in tunnel-based coordinates. The later times will be further upstream. In the contour plots, the color scale is kept constant for all measurements at a single Re. For these upstream measurements at z = 2.055 m, the contour levels were spaced every 0.005 p'/p_∞, and the zero pressure contour lines were removed. Measurements further downstream at z = 2.781 m had minimum contour lines at $\pm$ 0.05 p'/p_∞. Other contour lines were displayed at intervals of 0.1 p'/p_∞.

Fig. 9 shows these upstream measurements at a high Re of 10.8×10^6/m. Along the centerline (y = 0 mm), there is an initial positive pressure peak, followed by a low pressure dip and a second pressure peak. The peak amplitude of this low-frequency wave is 1.5–2% of the freestream pressure. The first high and low pressure regions extend in the spanwise direction and turn downstream. In contrast, the second pressure rise decays away from the centerline. The frequency content of the pressure disturbance is confined below 20 kHz. This result is surprising because repeatable second mode waves near 50 kHz are created by the perturber and measured further downstream. However, it appears that at this initial stage of the disturbance growth, high frequency second-mode waves have not grown enough to be measured above the electronic noise level, at least at the tunnel wall.

Fig. 10(a) show centerline time traces at this location and further downstream along the tunnel centerline. By z = 2.201 m, small second-mode waves are seen developing on top of the second positive pressure peak. Fig. 10(b) clearly shows a peak in the PSD near 45–50 kHz corresponding to the second mode-frequency. These waves continue to grow further downstream and develop into large second-mode instability wave packets before they break down into turbulent spots.[13,14] Because repeatable second-mode waves are generated and measured as early as z = 2.201 m, it seems likely that the second-mode frequencies are present further upstream but cannot be measured above the electronic noise. This is illustrated by considering five individual time traces of the disturbances at z = 2.055 m along with the ensemble average of all fifty time traces (Fig. 11). The signal is not much higher than the background electronic noise levels. The low-frequency portion of the disturbance can be readily seen, but it is not possible to resolve even smaller second-mode waves on top of this low frequency.

At a lower Re of 8.40×10^6/m, the disturbance development is similar (Fig. 12). There is once again a high-pressure region at the front of the disturbance that extends far in the spanwise direction. It is followed by a low-pressure region that has also begun to spread away from the centerline. These regions are followed by a second pressure peak that is largest at the center and decays away in the spanwise direction. Once again the frequency content of the disturbance extends up to ~20 kHz. Also, the second-mode wave frequencies cannot be resolved above the electronic noise level. However, further downstream, these second-mode waves appear on the second positive pressure peak (Fig. 13(a)) and are also observed in the PSD as a higher frequency peak near 40–45 kHz (Fig. 13(b)).

At the lowest Re of 6.40×10^6/m, a similar result is seen. However, instead of two pressure peaks, there is a single pressure rise with a small dip in the middle. The frequency content of the waves is lower and only extends to 10 kHz (Fig. 14(b)). Once again, it appears higher frequency second-mode waves cannot be measured about the electronic noise level, but they are seen further downstream as they grow (Fig. 14(a)). At this Re, a small peak near 35 kHz can be seen in the PSD as early as z = 2.201 m, corresponding to the second-mode waves (Fig. 14(b)).

These measurements show the initial development of disturbances in the boundary layer. While lower frequencies can be resolved, the higher frequency second-mode waves are too small to be measured at z = 2.055 m. It would be useful to make similar spanwise measurements further downstream in order to have spanwise data of the second-mode waves while they are still small and linear. However, there is no available location for another spanwise array of sensors between the upstream insert and the downstream pipe insert.

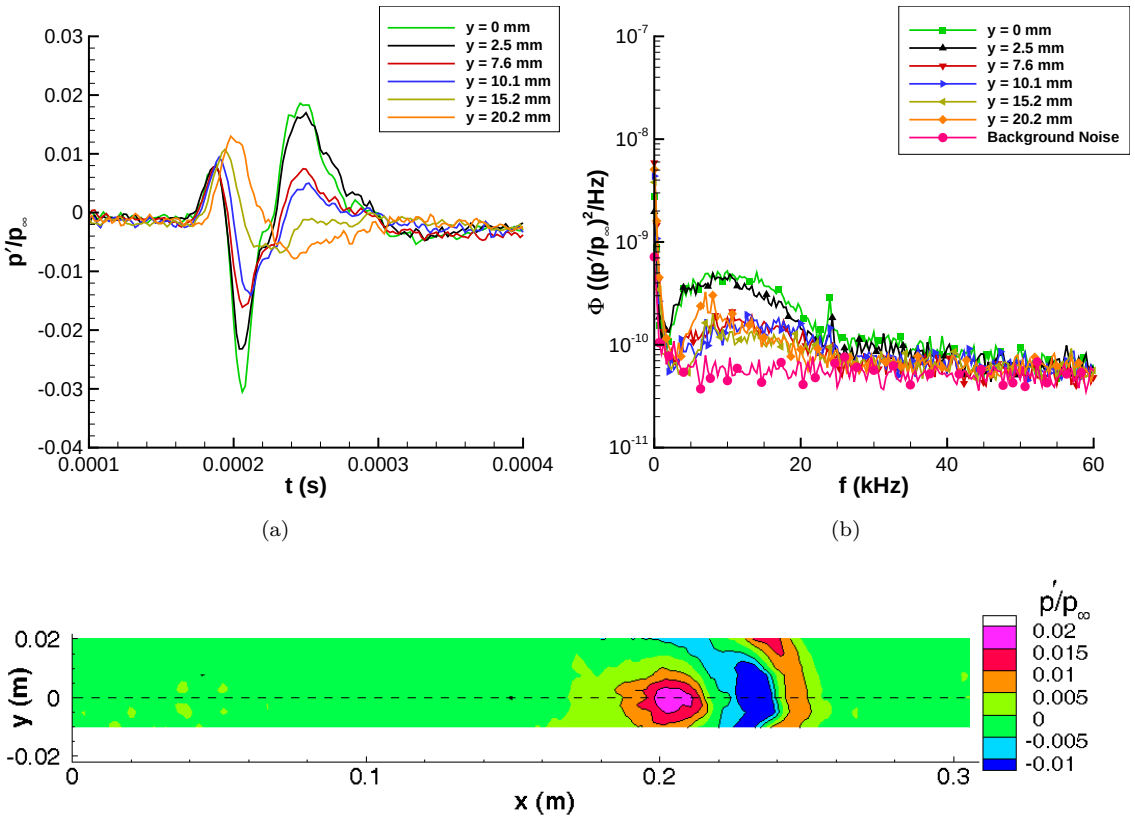

(a) (b)

(c)

Figure 9. Upstream disturbance measurements at $Re = 10.8 \times 10^6$/m, z = 2.055 m (a) Time traces; (b) Power-spectral density; (c) Contour plot.

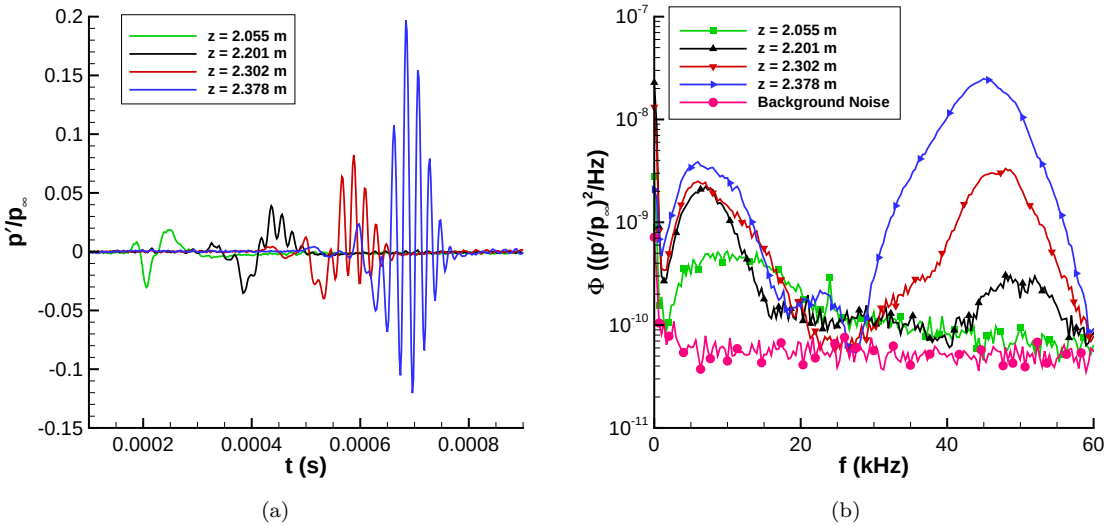

(a) (b)

Figure 10. Centerline disturbance measurements at $Re = 10.8 \times 10^6$/m, z = 2.055 m (a) Time traces; (b) Power-spectral density.

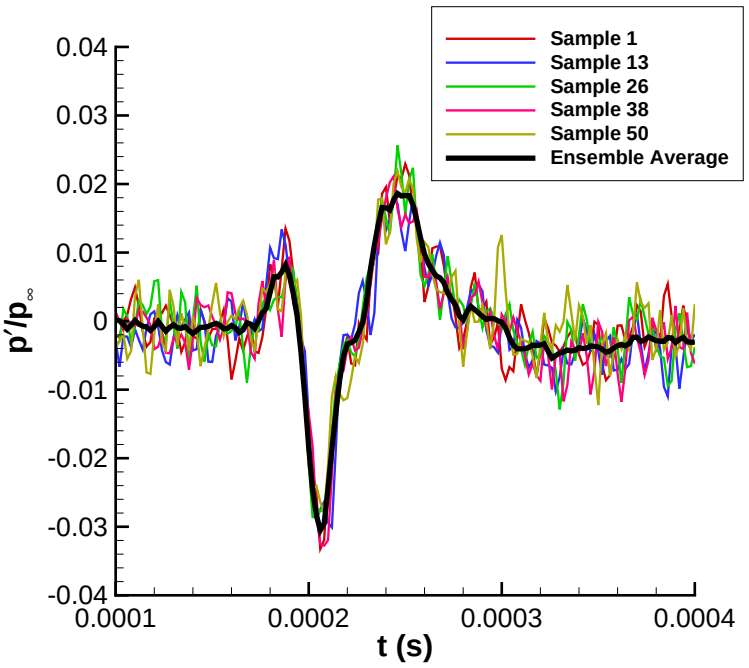

Figure 11. Comparison of individual disturbance time traces to ensemble average at $Re = 10.8 \times 10^6/m$, z = 2.055 m.

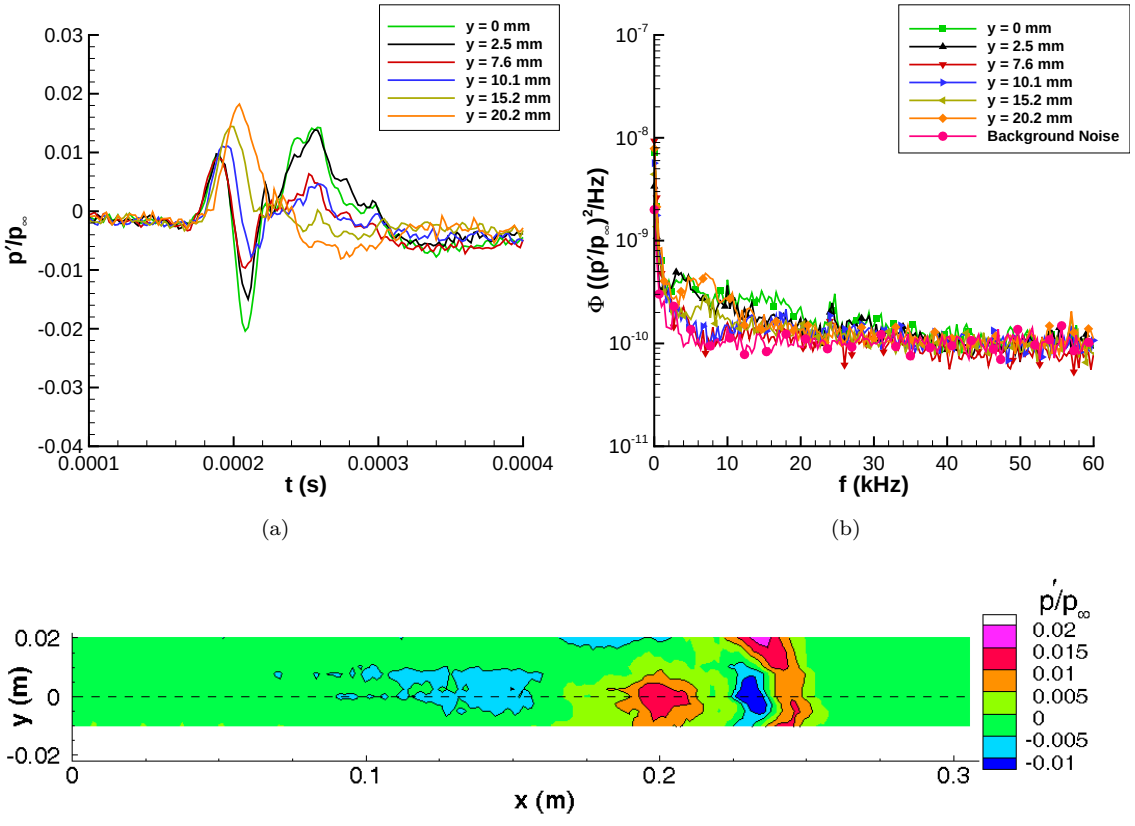

Figure 12. Upstream disturbance measurements at $Re = 8.40 \times 10^6/m$, z = 2.055 m (a) Time traces; (b) Power-spectral density; (c) Contour plot.

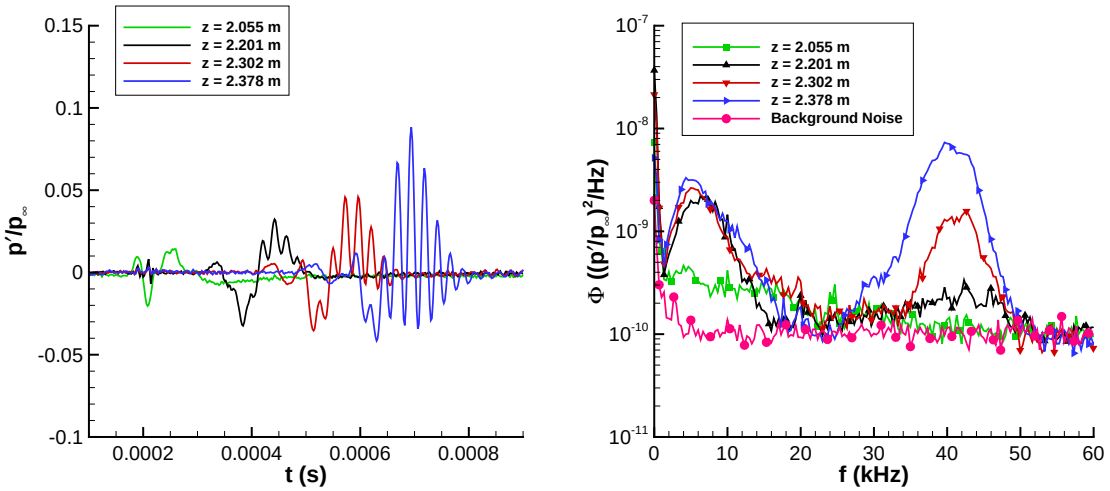

(a) (b)

Figure 13. Centerline disturbance measurements at $Re = 8.40 \times 10^6/m$, z = 2.055 m (a) Time traces; (b) Power-spectral density.

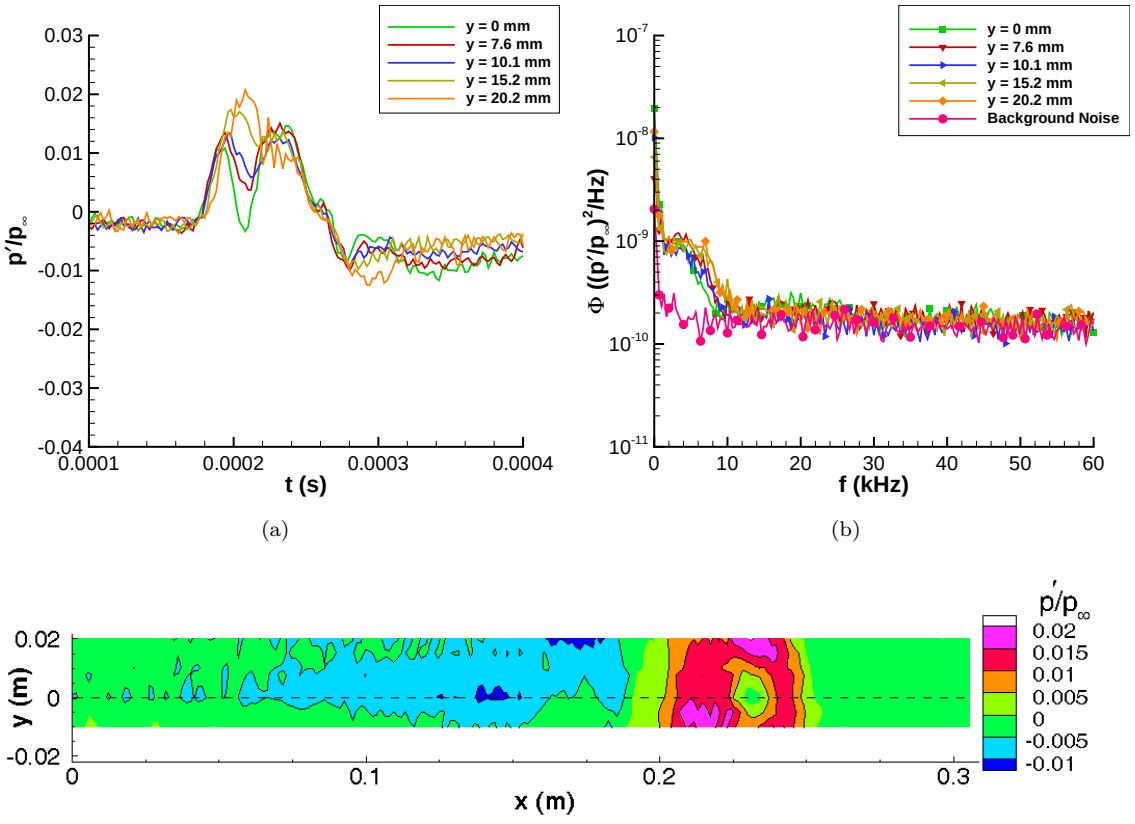

(a) (b)

(c)

Figure 14. Upstream disturbance measurements at $Re = 6.40 \times 10^6/m$, z = 2.055 m (a) Time traces; (b) Power-spectral density; (c) Contour plot.

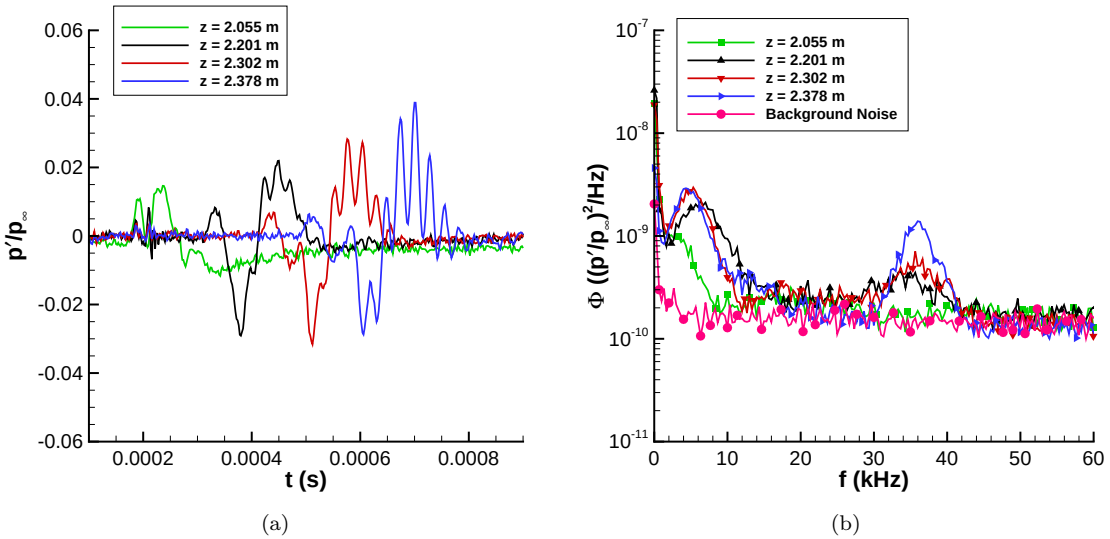

(a) (b)

Figure 15. Centerline disturbance measurements at $Re = 6.40 \times 10^6/m$, z = 2.055 m (a) Time traces; (b) Power-spectral density.

C. Repeatability of Controlled Disturbances

The repeatability of the perturbations and resulting disturbances is important for interpreting the results and comparing to DNS computations. The repeatability of individual time traces and ensemble averages was discussed in Ref. 13. It was shown that individual small disturbances repeat well, but as they become nonlinear and break down there is more variability from sample to sample. In all cases, the ensemble-averaged results still repeated well. In order to explore the sensitivity of the results to other factors, the electrode and electrode orientation were changed for some runs. Also, repeat runs were made without upstream sensor inserts to show that the sensors do not perturb the flow.

1. Repeatability of results with different electrodes

A single set of electrodes was typically used for all measurements. However, to show that the results were independent of the electrode and did not change with repeated use, a duplicate Macor electrode insert was fabricated. Tests were then repeated with this new electrode. Figure 16 shows a comparison of the results at a low Re of 6.40×10^6/m. The new electrode creates somewhat larger disturbances, but the overall time traces and frequency content of the disturbances are similar.

2. Repeatability of measurements with electrode rotation

Tests were also conducted to see if the orientation or polarity of the electrodes had a significant impact on results. Early tests indicated that the disturbances might not be symmetric about the centerline.[14] Instead, disturbances appeared symmetric about one of the electrodes, which would be consistent with a pulsed glow centered around one of the electrodes. Repeat runs were conducted with reversed electrode polarity ($\theta_e = 180°$). Also, the electrode was rotated by ninety degrees so that the electrode axis was in line with the freestream direction. Repeat runs were again conducted without ($\theta_e = 90°$) and with reversed polarity ($\theta_e = 270°$). Figs. 17(a) and 17(b) show comparisons of these different configurations along the centerline of the disturbance at z = 2.781 m. There is some scatter between each run, but the overall characteristics of the disturbances are similar. Off-center results at ± 11 mm are shown in Figs. 18(a) and 18(b). Some asymmetry is seen with the original configuration ($\theta_e = 0°$). However, when the polarity is switched, that asymmetry disappears for unknown reasons. This trend is not consistent with the glow discharge flipping to the other side of the centerline. Perhaps measurements are needed further upstream when the waves are smaller and more repeatable. When the perturber is rotated, no asymmetry is seen with either polarity. Overall, these results indicate that the rotation and polarity of the electrodes does not seem to have a significant effect on

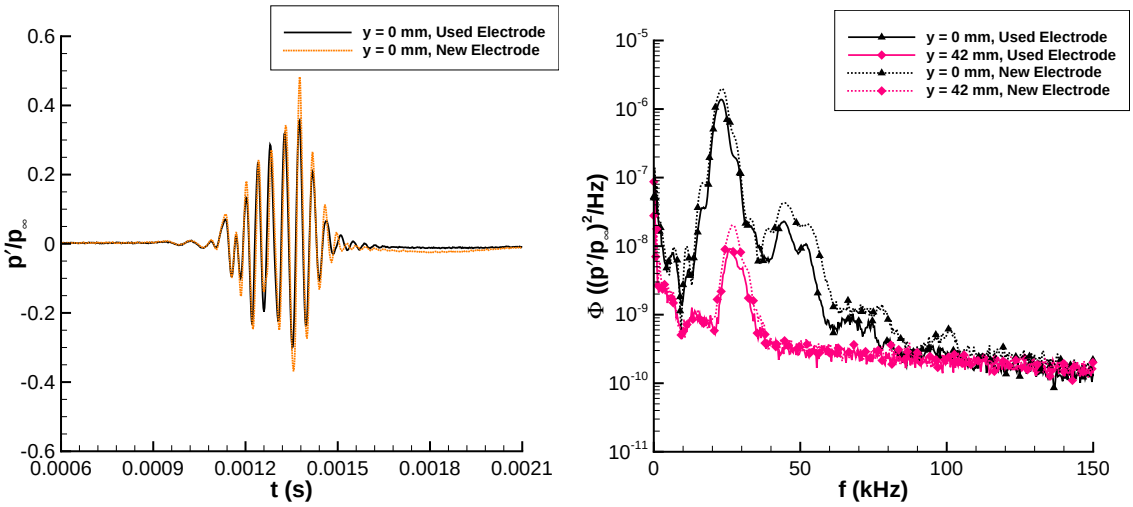

(a) (b)

Figure 16. Comparison of disturbances at z = 2.781 m with new and used electrodes, $Re = 6.40 \times 10^6$/m (a) Centerline time traces; (b) Power-spectral density.

the disturbances. However, future experiments should place the electrode gap in line with the freestream to eliminate possible asymmetry.

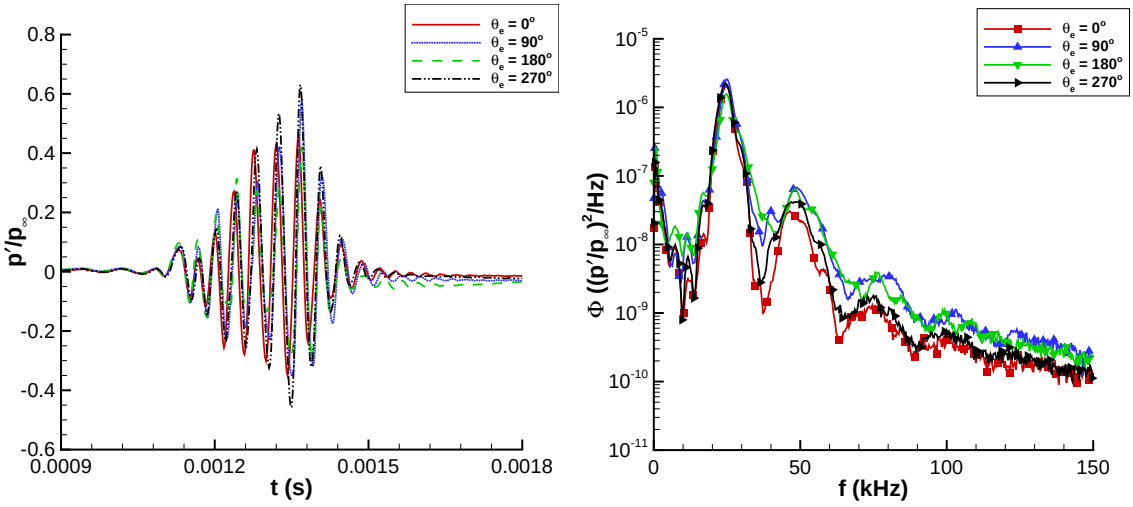

(a) (b)

Figure 17. Comparison of centerline disturbances at z = 2.781 m with electrode polarity switches and electrode rotation at $Re = 6.40 \times 10^6$/m (a) Time traces; (b) Power-spectral density.

3. Repeatability of measurements with no upstream sensor inserts

To ensure that the sensors themselves do not perturb the flow, repeat runs were made with and without upstream sensor blanks. The spanwise sensor insert at z = 2.055 m as well as a long traverse plug insert with sensors between z = 2.201 and 2.480 m were replaced with blank, contoured inserts. Figure 19 shows comparisons of repeat runs with and without these upstream blanks at varying *Re*. Repeatability of the results is good, indicating that the upstream sensors do not influence measurements further downstream.

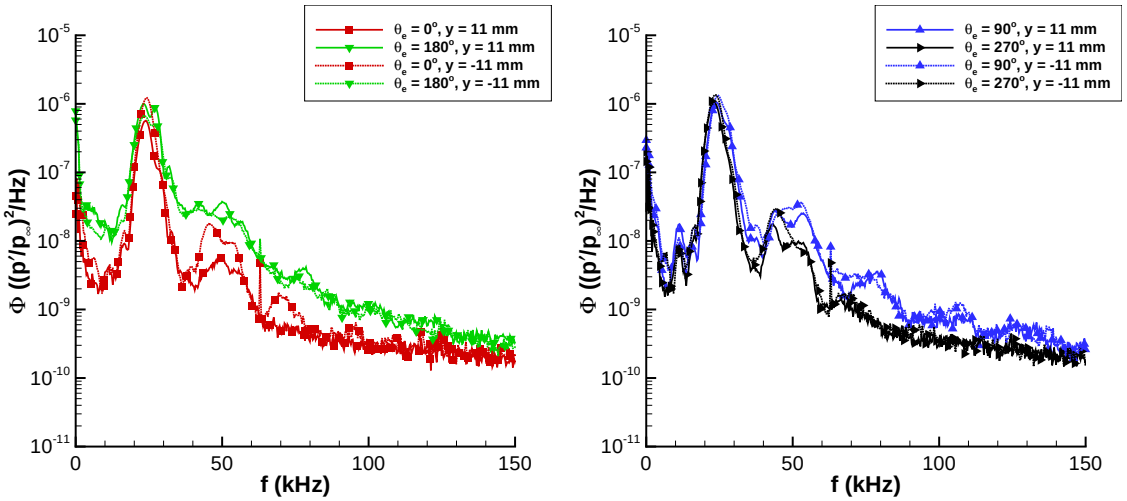

(a) (b)

Figure 18. Comparison of disturbances at z = 2.781 m and y = ± 11 mm with electrode polarity switches at $Re = 6.40 \times 10^6$/m (a) Power-spectral density with $\theta_e = 0°$ and $180°$; (b) Power-spectral density with $\theta_e = 90°$ and $270°$.

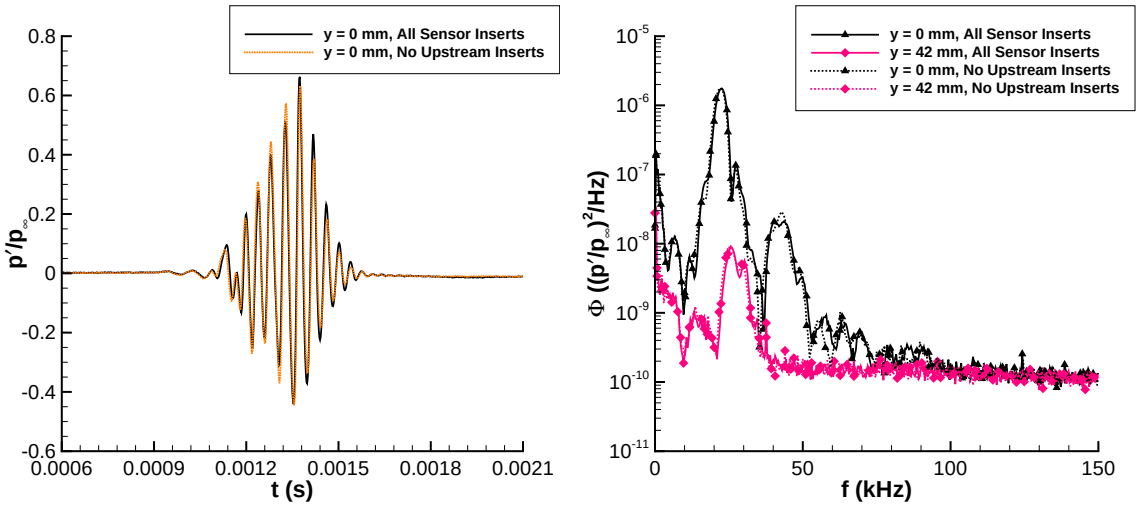

(a) (b)

Figure 19. Comparison of disturbances with and without upstream sensor inserts, $Re = 6.40 \times 10^6$/m (a) Time traces; (b) Power-spectral density.

D. Axisymmetry of the Nozzle-Wall Boundary Layer

The flow in the BAM6QT is typically assumed to be axisymmetric because the nozzle is precisely machined, and the tunnel is carefully aligned. However, there are other factors that might cause asymmetry. A check of the axisymmetry of the nozzle-wall flow was tested by rotating the entire setup by 180 degrees. Fig. 20(a) shows time traces of spanwise measurements at z = 2.781 m on the top ($\theta = 0°$) and bottom ($\theta = 180°$) walls at $Re = 6.40 \times 10^6$/m. There are differences between the two measurements. The instability waves are larger on the bottom wall compared to the top wall. Also, the wave packet on the bottom wall of the tunnel is accompanied by a large low pressure region. This region extends downstream almost until the following perturbation is generated at t = 0.005 s. This low-pressure region is significantly larger than the region on the top wall of the tunnel, which can barely be seen at this Re. This region on the top wall only becomes apparent at higher Re. Also, the frequency of the unstable waves is approximately 15–20% higher on the bottom wall. This can be seen in the shorter duration of the high-frequency portion of the wave packet and is also apparent in the PSD of the time traces (Fig. 20(b)). This higher frequency implies that the boundary layer is ∼8–10% thinner on the bottom wall compared to the top wall. The waves are also larger on the bottom wall of the tunnel.

At higher Re, the waves grow and break down further upstream; however, the trends are the same as at lower Re (Fig. 21). The waves are larger on the bottom wall compared to the top wall, and the top wall has a slightly lower instability frequency than the bottom wall. There is again a very large low pressure region behind the disturbances on the bottom wall, which continues until the next disturbance is generated. At higher Re, it extends into the following disturbance. Disturbances on the bottom wall would need to be generated at frequencies much lower than 200 Hz in order for this low pressure region to decay away before introducing a second perturbation.

As the packets break down to turbulence, the difference between the top and bottom walls decreases. Fig. 22 shows the evolution of centerline disturbances at z = 2.730 m for increasing Re on the top and bottom walls of the tunnel. Even though there is a shift in the peak frequency of the instability waves and the waves develop faster on the bottom wall of the tunnel, the evolution of the disturbances as they grow and break down is similar on the top and bottom wall.

These differences are consistent with temperature stratification in the tunnel.[20] Because the driver-tube and contraction air must be heated to avoid condensation during a wind-tunnel run, there is inherent free convection and temperature stratification in the driver tube. However, the nozzle is not heated. When the air passes from the contraction and through the throat, tunnel bleeds remove ∼30% of the air and start a new boundary layer at the throat. However, some of this stratification will remain in the tunnel, and the top wall of the tunnel will be hotter than the bottom of the tunnel. This means that the density will be lower on the top wall of the tunnel, resulting in a thicker boundary layer and lower second-mode wave frequencies. This stratification can also affect the stability of the boundary layer. Second-mode waves are more unstable on a cooled wall.[21–24]

In order to investigate the temperature stratification in the BAM6QT, a Medtherm type-E coaxial thermocouple was placed in the pipe insert at z = 2.755 m. Measurements of the wall temperature were made prior to a run during several days of testing (Fig. 23). The temperature typically increases by 0.5 – 2 K from run to run. Larger temperature increases are seen earlier in the day. Smaller increases occur for later tunnel runs once the wall temperature has already increased. Decreases in the average temperature are usually seen only when there is a long period of time between runs. The temperature stratification in the tunnel also shows up in these measurements. The top wall of the tunnel has a consistently higher temperature than the bottom wall. This temperature difference is near 4 K for the first run in a day. However, the top wall of the tunnel heats up more than the bottom wall throughout the day. After a full day of testing, the temperature difference between the top and bottom wall of the tunnel at z = 2.755 m is near 9 K. This means that the top wall of the tunnel is approximately 3% hotter than the bottom wall at this location.

The trends in instability wave growth and frequency are consistent with temperature stratification in the tunnel. However, it is surprising that a wall temperature change of 3% could change the results so much. In order to investigate this further, the Harris Boundary-Layer Code[25] was used to compute the boundary layer near $Re = 5.80 \times 10^6$/m[26] with and without a 3% temperature increase. Computations showed a change in boundary layer thickness of only 2% at the downstream end of the nozzle, not 8–10% as implied by the second-mode wave measurements. However, these computations make many assumptions. The wall-temperature distribution was found by measuring the external temperature of the nozzle and using a finite-element code to compute the internal nozzle-wall temperature.[27] In order to improve the accuracy

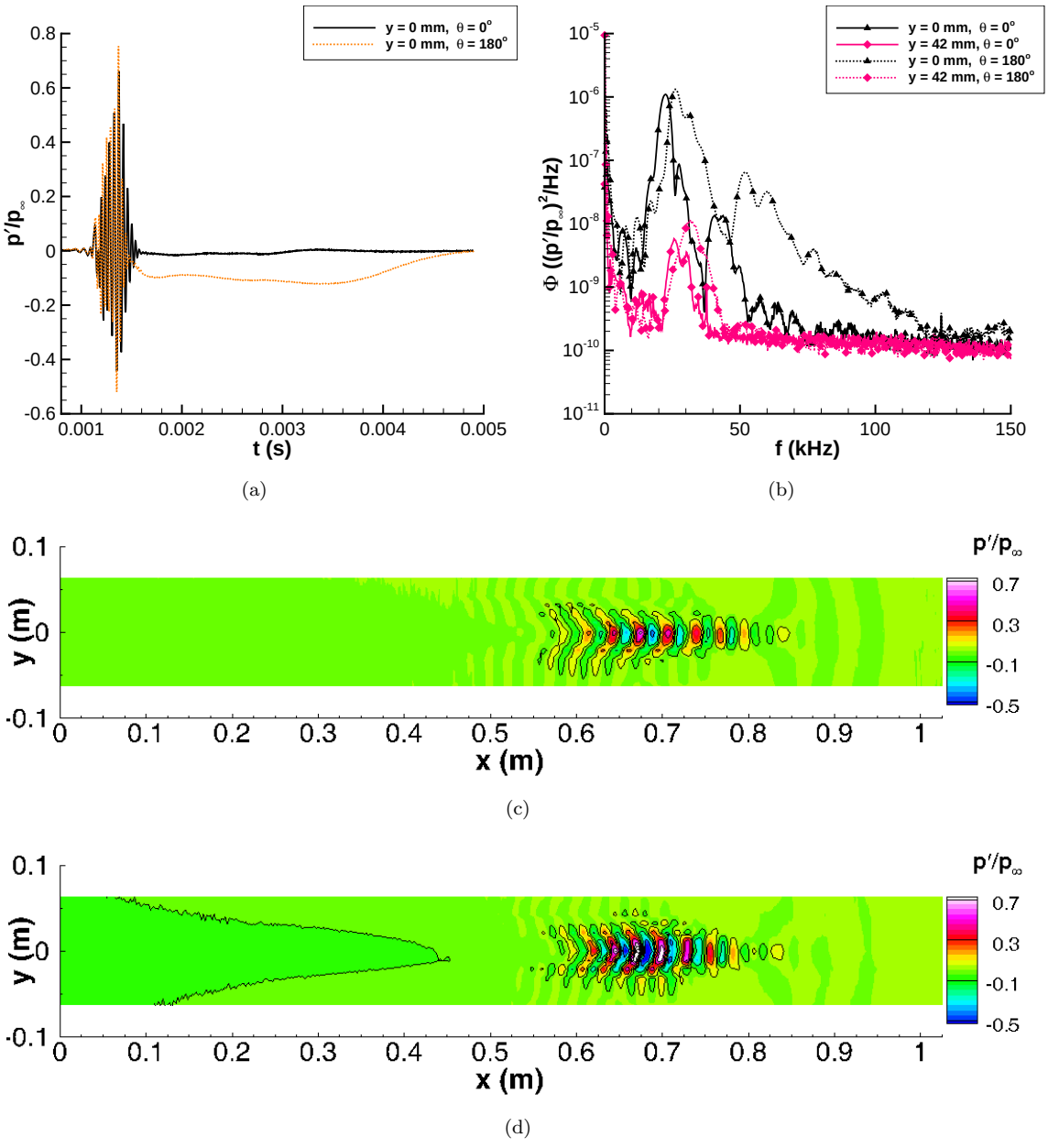

Figure 20. Comparison of disturbances on top and bottom wall of the tunnel at z = 2.781 m, $Re = 6.40 \times 10^6$**/m (a) Centerline time traces; (b) Power-spectral density; (c) Contour plot on top wall; (d) Contour plot on bottom wall.**

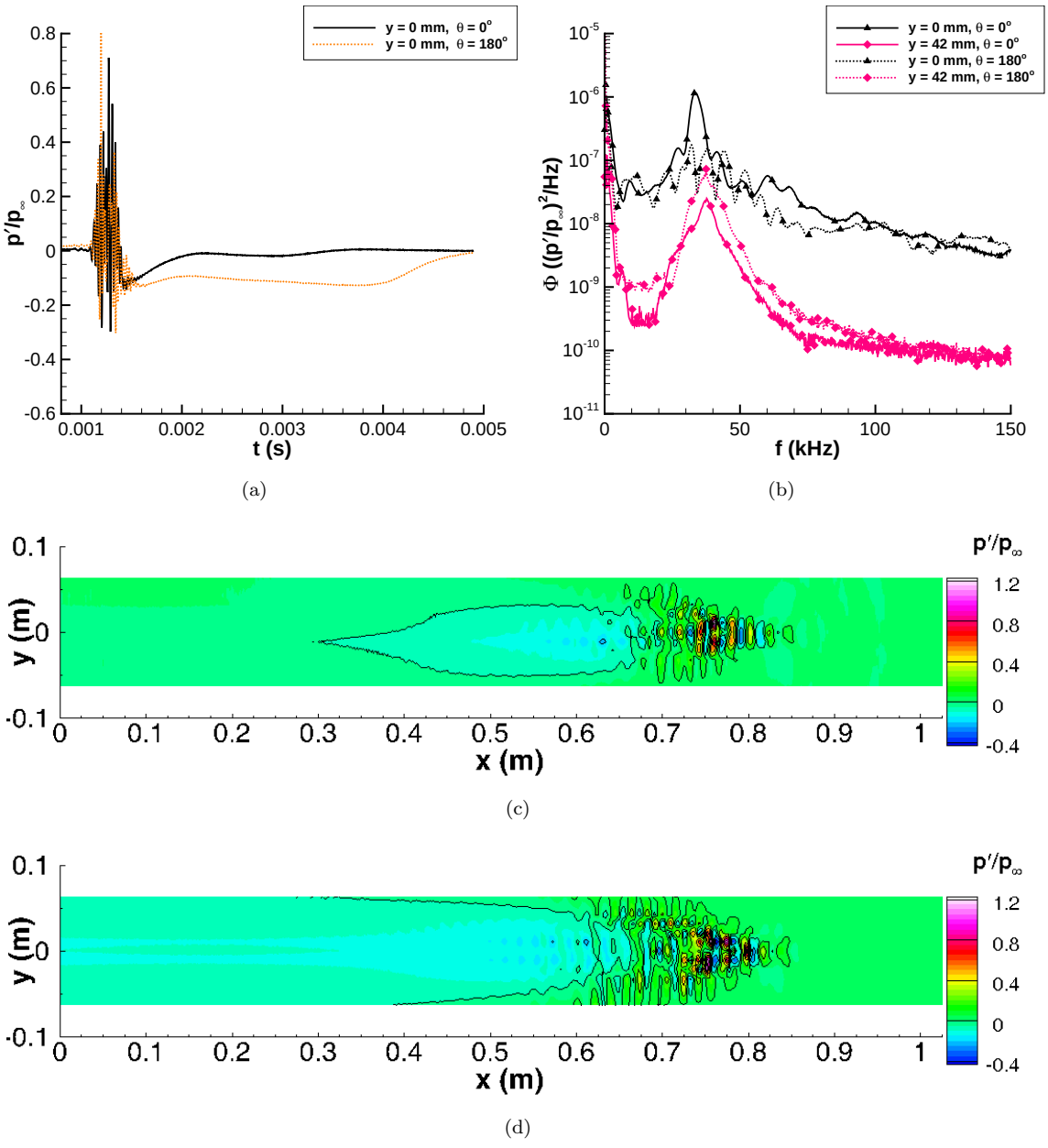

Figure 21. Comparison of disturbances on top and bottom wall of the tunnel at z = 2.781 m, $Re = 8.40 \times 10^6$**/m (a) Centerline time traces; (b) Power-spectral density; (c) Contour plot on top wall; (d) Contour plot on bottom wall.**

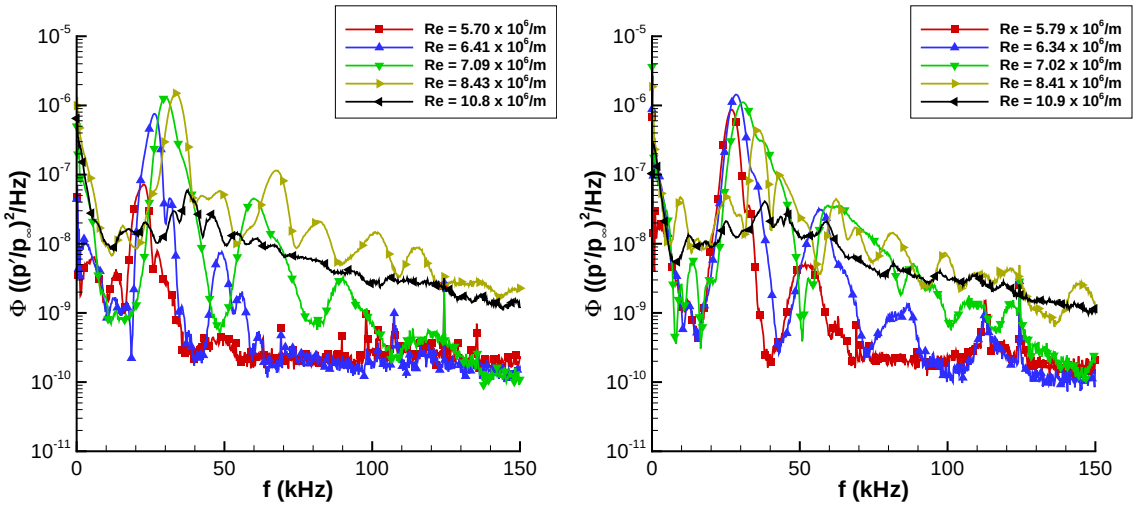

(a) (b)

Figure 22. Comparison of centerline disturbances on top and bottom wall of the tunnel at z = 2.730 m (a) Top wall; (b) Bottom wall.

of the computations, measurements of wall temperature are needed at more points along the nozzle and should be compared to the assumed temperature profile. It would also be interesting to see how large of a wall-temperature effect is seen in DNS computations.

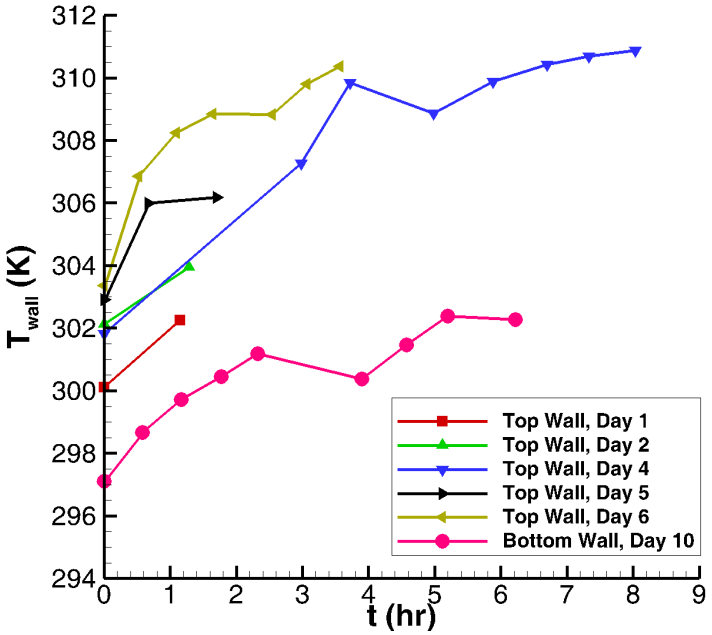

Figure 23. Increase in average wall temperature at z = 2.755 m throughout a testing day, each point corresponds to a tunnel run.

IV. Concluding Remarks

Better characterization of the controlled perturber experiments on the nozzle wall of the BAM6QT was conducted. The voltage and current of the perturber were measured, and the electrodes were imaged during the perturbation generation. These showed that the perturbation is actually a pulsed glow discharge, not an arc discharge, although sparks do occasionally occur along with a glow pulse. However, because of the electrical noise generated by the spark and the non-repeatability of this arc discharge, data from the combined spark-glow perturbation are not used. It appears that the dominant frequencies of the glow perturbation are below 30 kHz, though there are also low levels of higher frequency content. It is still unclear how the electrical perturbation couples with the flow to generate controlled disturbances in the boundary layer.

In order to better characterize the near-field of the perturber, a spanwise array of sensors at z = 2.055 m was used to measure the small disturbances before they become nonlinear and break down to turbulence. A high and low pressure disturbance was measured that extends far in the spanwise direction. Behind this disturbance, a low-frequency positive pressure peak is concentrated near the centerline. At this location, high-frequency second-mode waves are not seen. These waves are likely too small to be measured above the electronic noise in the tunnel. However, they are observed further downstream growing on this second pressure peak.

Measurements of the repeatability of experiments were also made. Experiments were repeated with different electrodes and electrode polarity. Also, the perturber was rotated 90 degrees, in line with the freestream. In order to verify that the pressure sensors did not perturb the flow, upstream sensor inserts were removed and replaced by contoured blanks. In all cases, similar results were obtained. Finally, the setup was switched to the bottom wall of the tunnel to check the axisymmetry of the nozzle-wall boundary layer. The second-mode waves occurred at 15–20% higher frequencies and also grew more quickly. These frequency differences imply a change in boundary-layer thickness of 8–10%. These trends are consistent with the temperature stratification in the tunnel. At z = 2.755 m, the top wall of the tunnel was found to be ∼3% hotter than the bottom wall. However, initial computations with and without a 3% increase in the nozzle-wall temperature profile only accounted for a 2% change in boundary-layer thickness. A more accurate profile along the nozzle wall is needed to explore this asymmetry further.

Acknowledgments

This work could not have been completed without the help of John Phillips, the Purdue AAE department electronics technician, who designed and built the perturber used for these measurements. Peter Gilbert provided the CAD model used to generate Fig. 2. Dr. Sally Bane suggested the use of the current transformer for characterizing the perturbations. Funding was provided in part by the National Science Foundation Graduate Research Fellowship Program, Sandia National Laboratories, and AFOSR.

References

[1]Laganelli, A. L., Martellucci, A., and Shaw, L. L., "Wall Pressure Fluctuations in Attached Boundary-Layer Flow," *AIAA Journal*, Vol. 21, No. 4, 1983, pp. 495–502.

[2]Pate, S. R. and Brown, M. D., "Acoustic Measurements in Supersonic Transitional Boundary Layers," AEDC-TR-69-182, October 1969.

[3]Johnson, R. I., Macourek, M. N., and Saunders, H., "Boundary Layer Acoustic Measurements in Transitional and Turbulent Flow at $M_\infty = 4.0$," AIAA Paper 69-344, April 1969.

[4]Cassanto, J. M. and Rogers, D. A., "An Experiment to Determine Nose Tip Transition with Fluctuating Pressure Measurements," *AIAA Journal*, Vol. 13, No. 10, October 1975, pp. 1257–1258.

[5]Martellucci, A., Chaump, L., Rogers, D., and Smith, D., "Experimental Determination of the Aeroacoustic Environment about a Slender Cone," *AIAA Journal*, Vol. 11, No. 5, 1973, pp. 635–642.

[6]Pate, S. R., "Dominance of Radiated Aerodynamic Noise on Boundary-Layer Transition in Supersonic/Hypersonic Wind Tunnels," AEDC-TR-77-107, March 1978.

[7]Narasimha, R., "The Laminar-Turbulent Transition Zone in the Boundary Layer," *Progress in Aerospace Sciences*, Vol. 22, January 1985, pp. 29–80.

[8]Park, S. and Lauchle, G., "Wall Pressure Fluctuation Spectra Due to Boundary-Layer Transition," *Journal of Sound and Vibration*, Vol. 319, 2009, pp. 1067–1082.

[9]Krishnan, L. and Sandham, N. D., "Effect of Mach Number on the Structure of Turbulent Spots," *Journal of Fluid Mechanics*, Vol. 566, 2006, pp. 225–234.

[10]Joksch, A. and Kleiser, L., "Growth of Turbulent Spots in High-Speed Boundary Layers on a Flat Plate," *International Journal of Heat and Fluid Flow*, Vol. 29, 2008, pp. 1543–1557.

[11]Sivasubramanian, J. and Fasel, H. F., "Direct Numerical Simulation of a Turbulent Spot in a Cone Boundary-Layer at Mach 6," AIAA Paper 2010-4599, June 2010.

[12]Sivasubramanian, J. and Fasel, H. F., "Transition Initiated by a Localized Disturbance in a Hypersonic Flat-Plate Boundary Layer," AIAA Paper 2011-374, January 2011.

[13]Casper, K., Beresh, S., and Schneider, S., "Pressure Fluctuations Beneath Turbulent Spots and Instability Wave Packets in a Hypersonic Boundary Layer," AIAA Paper 2011-372, January 2011.

[14]Casper, K., Beresh, S., and Schneider, S., "Spanwise Growth of the Turbulent Spot Pressure-Fluctuation Field in a Hypersonic Boundary Layer," AIAA Paper 2011-3873, June 2011.

[15]Keyes, F. G., "A Summary of Viscosity and Heat-Conduction Data for He, A, H_2, O_2, N_2, CO, CO_2, H_2O, and Air," *Transactions of the ASME*, Vol. 73, July 1951, pp. 589–596.

[16]Steen, L. E., *Characterization and Development of Nozzles for a Hypersonic Quiet Wind Tunnel*, Master's Thesis, Purdue University School of Aeronautics & Astronautics, December 2010.

[17]Schneider, S. P., "The Development of Hypersonic Quiet Tunnels," *Journal of Spacecraft and Rockets*, Vol. 45, No. 4, 2008, pp. 641–664.

[18]Beresh, S. J., Henfling, J. F., Spillers, R. W., and Pruett, B. O. M., "Measurements of Fluctuating Wall Pressures Beneath a Supersonic Turbulent Boundary Layer," AIAA Paper 2010-305, January 2010.

[19]Rotea, M. A., Randall, L. A., Song, G., and Schneider, S. P., "Model Identification of a Kulite Pressure Transducer," Paper 96-2278, AIAA, June 1996.

[20]Borg, M. P., *Characteristics of the Contraction of the Boeing/AFOSR Mach-6 Quiet Tunnel*, Master's Thesis, Purdue University School of Aeronautics & Astronautics, December 2005, Available from DTIC as ADA441151.

[21]Mack, L. M., "Linear Stability Theory and the Problem of Supersonic Boundary-Layer Transition," *AIAA Journal*, Vol. 13, No. 3, 1975, pp. 278–289.

[22]Demetriades, A., "New Experiments on Hypersonic Boundary Layer Stability Including Wall Temperature Effects," *Proceedings of the Heat Transfer and Fluid Mechanics Institute*, 1978, pp. 39–55.

[23]Mack, L. M., "Boundary Layer Linear Stability Theory," *Report 709, Special Course on Stability and Transition of Laminar Flow*, AGARD, March 1984, pp. 1–81.

[24]Stetson, K. F. and Kimmel, R. L., "Surface Temperature Effects on Boundary-Layer Transition," *AIAA Journal*, Vol. 30, No. 11, 1992, pp. 2782–2783.

[25]Harris, J. and Blanchard, D., "Computer Program for Solving Laminar, Transitional, or Turbulent Compressible Boundary-Layer Equations for Two-Dimensional and Axisymmetric Flow," Tech. Rep. NASA-TM-83207, NASA, February 1982.

[26]Ward, C. A. C., Wheaton, B., Chou, A., Berridge, D. C., Letterman, L. E., and Schneider, S. P., "Hypersonic Boundary-Layer Transition Experiments in the Boeing/AFOSR Mach-6 Quiet Tunnel," AIAA Paper, To appear, January 2012.

[27]Skoch, *Final Assembly and Initial Testing of the Purdue Mach-6 Quiet-Flow Ludwieg Tube*, Master's Thesis, Purdue University School of Aeronautics & Astronautics, December 2001.